EES Solar

PAPER

View Article Online
View Journal | View Issue

Cite this: *EES Sol.*, 2025, **1**, 331

An interfacial degradation mechanism in inverted perovskite solar cells with a sol–gel derived NiO_x hole transport layer†

Abraha Tadese Gidey, *[abc] Elias Assayehegn,[c] Esayas Alemayehu,[d] Alexander R. Uhl [b] and Jung Yong Kim *[ef]

Received 9th April 2025
Accepted 15th April 2025

DOI: 10.1039/d5el00057b

rsc.li/EESSolar

NiO_x-based inverted perovskite solar cells (PSCs) exhibit desirable stability and efficiency potential. However, their long-term stability remains a significant concern necessitating the investigation of interfacial stability and degradation mechanisms. Hence, the present study offers a pragmatic comprehension of the degradation pathways of the perovskite ($CH_3NH_3PbI_3$) layer under environmental stressors. For this purpose, the sol–gel-derived NiO_x-based inverted PSCs were exposed to moisture, oxygen, and heat energy at four different stages of device fabrication. Then, the macroscopic visual image, optical absorption, X-ray diffractograms, and device performance decays were analyzed for these layer-by-layer (LBL) structural samples. Consequently, it was found that the rapid degradation of the inverted PSCs with a NiO_x hole transport layer under humidity, air, and thermal stresses was primarily related to silver diffusion into the perovskite layer and the irreversible breakdown of perovskite into its precursors. Furthermore, the performance of the NiO_x layer for versatile perovskite materials was studied *via* composition engineering (*i.e.*, mixed cation and anion systems). This work may provide practical insight for improving our understanding of device stability, paving the way for commercialization.

Broader context

Halide perovskites with a general chemical structure of ABX_3 (A = CH_3NH_3, $CH(NH_2)_2$ and Ce; B = Pb and Sn; and X = I, Br and Cl) have received great attention as next-generation semiconductors for optoelectronics including solar cells, light-emitting diodes, field-effect transistors, *etc.* Specifically, the power conversion efficiency of perovskite solar cells (PSCs) has already reached over 26%, demonstrating their competitive edge with low-cost solution processability. The performance of PSCs is based on the excellent properties of perovskites such as high absorption coefficients, long charge diffusion length, defect tolerance, high charge mobility, tunable bandgaps, *etc.* However, considering the 'golden triangle' of solar cells (*i.e.*, efficiency, cost, and lifetime), the stability of PSCs should be a key factor in the current research and development (R&D) stages. Hence, this work is devoted to elucidating the interfacial stability and degradation mechanisms in the sol–gel derived NiO_x–based inverted PSCs under moisture, oxygen, and thermal exposure. For this purpose, the stability of PSCs was studied at four different stages of device fabrication *via* a layer-by-layer approach, laying the foundations for commercial viability.

1. Introduction

Perovskite solar cells (PSCs) are emerging photovoltaic technologies that utilize halide perovskite semiconductors with versatile dimensions and nanoscale shapes for optoelectronics application.[1–6] Currently, the single-junction PSCs reached a power conversion efficiency (PCE) of over 26%.[7–10] Despite their impressive efficiency, the instability of PSCs remains a serious concern towards commercialization.[11] PSCs tend to degrade when exposed to humidity, heat, light, and electric fields.[12,13] This instability is due to the chemical reactions being initiated in the presence of oxygen and water, and ion migration *via* defect sites causes the structural instability of perovskite semiconductors.[14,15] Interestingly, the stability of PSCs is also dependent on the device architecture of PSCs such as an inverted or regular structure.[16–25]

[a]*Faculty of Materials Science and Engineering, Jimma Institute of Technology, Jimma University, P.O. Box 378, Jimma, Ethiopia. E-mail: Abraha.tadesse@mu.edu.et*
[b]*Laboratory for Solar Energy and Fuels (LSEF), School of Engineering, The University of British Columbia, Kelowna V1V1V7, Canada*
[c]*Department of Chemistry, College of Natural and Computational Sciences, Mekelle University, P.O. Box 231, Mekelle, Ethiopia*
[d]*Faculty of Civil and Environmental Engineering, Jimma Institute of Technology, Jimma University, P.O. Box 378, Jimma, Ethiopia*
[e]*Department of Materials Science and Engineering, Adama Science and Technology University, P.O. Box 1888, Adama, Ethiopia. E-mail: jungyong.kim@astu.edu.et*
[f]*Center of Advanced Materials Science and Engineering, Adama Science and Technology University, P.O. Box 1888, Adama, Ethiopia*

† Electronic supplementary information (ESI) available. See DOI: https://doi.org/10.1039/d5el00057b

Inverted PSCs offer multiple benefits compared to conventional structures, including easier fabrication, enhanced stability, reduced hysteresis, and lower energy loss.[16–25]

For further enhancing the stability of inverted configurations, the influence of each layer on the deterioration of devices should be elucidated.[26,27] These constituent layers include not only perovskite itself, but also other components such as the hole transport layer (HTL), electron transport layer (ETL), and electrodes. Nickel oxide (NiO_x) and fullerene derivative [6,6]-phenyl-C_{61}-butyric acid methyl ester (PCBM) are a typical HTL and ETL, respectively, in the inverted PSCs. Sol–gel derived NiO_x is a robust HTL suitable for perovskite with varied compositions and bandgaps as well as for various forms of substrates including those with textured structures.[28]

Among the primary degradation sources mentioned above, moisture ingress could result in perovskite decomposition, electrode corrosion, and delamination of interface layers, which could be further exacerbated by thermal stress.[29,30] In addition to environmental factors, the lifetime of inverted PSCs is affected by their intrinsic behavior. Intrinsic properties (hygroscopicity, thermal instability, and ion migration) could be coupled with extrinsic sources (humidity, heat, and electric field) and accelerate the perovskite deterioration.[31,32] The stability of PSCs could be affected by both the layer-by-layer (LBL) interface and bulk thin-film materials as well.[33,34] For outdoor applications, the accumulated heat in PSCs may increase the internal temperature to as high as 85 °C.[7]

In the regular PSCs, it has been widely reported that the organic HTL, 2,2′,7,7′-tetrakis[*N*,*N*-di(4-methoxyphenyl)amino]-9,9′-spirobifluorene (spiro-OMeTAD) mainly affects the degradation of perovskite. Besides, the introduction of additives such as 4-*tert*-butylpyridine (*t*BP) and bis-(trifluoromethane)sulfonimide lithium salt (Li-TFSI) can further accelerate the deterioration of the perovskite/HTL interface and materials.[35] Various studies have been reported on the degradation mechanisms of PSCs.[36–40] However, in the inverted PSCs, little research has been conducted to elucidate the effect of each layer on device stability in the presence of environmental stresses.

Herein, we comprehensively explore the influence of each layer on the stability of inverted PSCs with the sol–gel derived NiO_x HTL under moisture and thermal stresses. For this purpose, four kinds of device structures were constructed. To the best of the authors' knowledge, this study represents the first investigation of LBL stability analysis by constructing various half and full-device configurations. Our finding reveals that under environmental stressors, both the intrinsic perovskite properties and silver electrode diffusion are mainly attributed to the device degradation while the nanocrystalline[41] PCBM contributes positively toward device stability due to its relatively low water affinity and high glass transition temperature.[42] Finally, we provide a way forward for the enhanced stability of inverted PSCs.

2. Materials and methods

2.1 Materials

The chemicals and silver metal were used as received without further purification, including PbI_2 (>98%, TCI), methylammonium iodide (MAI, >98%, TCI), dimethyl sulfoxide (DMSO, 99.8%, Sigma-Aldrich), *N*,*N*-dimethylformamide (DMF, 99.8%, Sigma-Aldrich), isopropyl alcohol (IPA, 99.8%, Riedel-de Haën), Ag slug (99.9%, Gredmann), chlorobenzene (99.9%, Sigma-Aldrich), ethanol (99.8%, Riedel-de Haën), nickel(II) acetate ($Ni(OAc)_2$) tetrahydrate (98%, Showa), monoethanolamine (MEA, 99.7%, J.T. Baker), phenyl-C_{61}-butyric acid methyl ester (PCBM, 99.5%, U.R. Chemicals), and [2-(3,6-dimethoxy-9*H*-carbazol-9-yl) ethyl]phosphonic acid (MeO-2PACz, TCI). The dried solvents were stored over 4 Å molecular sieves before use. Fluorine doped tin oxide (FTO)-coated glass substrates with a sheet resistance of 15 Ω sq^{-1} were used for the present study.

2.2 Methods

The optical properties of the samples were measured using an ultraviolet-visible (UV-vis) absorption spectrophotometer (Hewlett Packard 8453). For analyzing the optical and crystallographic properties of the as-prepared samples, a perovskite film was deposited on FTO and FTO/NiO_x. The X-ray diffraction (XRD) patterns were obtained using a Bruker AX D8 Advance diffractometer with Cu Kα radiation ($\lambda = 1.5406$ Å). The work function of the NiO_x thin films was measured using an AC-2 photoelectron spectrometer (RIKEN KEIKI CO., LTD). A Veeco Dektak 150 surface profiler was employed to measure the film thicknesses. The wettability of FTO, NiO_x, and perovskite films was investigated by using a MICK, OCA 50 for water contact angle measurement. Tapping mode atomic force microscopy (AFM) images were obtained using a Veeco Dilnnova Atomic Force Microscope.

2.3 Thin film and device fabrication processes

NiO_x was prepared as a HTL through the sol–gel method, utilizing nickel(II) acetate tetrahydrate as the Ni(II) precursor and monoethanolamine (MEA) as a coordinating ligand in ethanol as the solvent, as illustrated in Fig. S1 in the ESI.† To fabricate NiO_x films, FTO/glass substrates were etched with hydrochloric acid (4 mol per L HCl) first and then cleaned with detergent mixed in deionized water, deionized water, acetone and isopropanol sequentially by sonicating for 15 min each. The cleaned FTO/glass substrates were then treated under UV-ozone for 15 min following blowing with strong nitrogen.

0.5 M NiO_x precursor solutions were prepared by dissolving nickel(II) acetate tetrahydrate and monoethanolamine with an equimolar stabilizer in anhydrous solvent. The solutions were then stirred at 70 °C for 45 min. The sol–gel sample turned to colorful green solutions, indicating the formation of a nickel–ligand complex. The colorful solutions were then filtered through 0.45 μm polyvinylidene fluoride (PVDF) filters before use. The NiO_x thin films were deposited on top of a glass/FTO substrate at 4000 rpm for 30 s using the NiO_x precursor sol–gel and annealed at 400 °C for 30 min.

For depositing the $MAPbI_3$ ($MA = CH_3NH_3$) perovskite active layers over FTO and FTO/NiO_x, the UV-ozone treated FTO and FTO/NiO_x substrates were transferred into a glovebox filled with nitrogen. The perovskite precursor solution was prepared by dissolving 461 mg PbI_2 and 159 mg of CH_3NH_3I in *ca.* 0.7 mL of

DMF/DMSO (=9 : 1 by volume ratio) and stirring at 80 °C for 2 h and then spin-coating on to the substrates *via* the one-step deposition technique at 3000 rpm for 25 s. 200 μL of anhydrous chlorobenzene was rapidly dropped on top of the substrates at the 10th s. The perovskite-spin-coated substrates were heated at 100 °C for 10 min to prepare FTO/$MAPbI_3$ and FTO/NiO_x/$MAPbI_3$ films. For fabricating FTO/NiO_x/$MAPbI_3$/PCBM samples, PCBM in chlorobenzene (20 mg mL^{-1}) was deposited at 2500 rpm for 15 s.

For fabricating a full device with an inverted structure of FTO/NiO_x/$MAPbI_3$/PCBM/Ag, an 80 nm thick silver layer was thermally deposited on top of the PCBM layer. The thicknesses of NiO_x, $MAPbI_3$, PCBM, and Ag were 30 nm, 450 nm, 40 nm, and 80 nm, respectively. The active area of the solar cell is 0.04 cm^2.

For evaluating the influence of self-assembled monolayer (SAM) modification on the performance of NiO_x-based PSCs, MeO-2PACz solution (0.3 mg mL^{-1} in ethanol) was spin-coated over the NiO_x layer at 3000 rpm for 30 s, following annealing at 100 °C for 10 min. Then the film was washed with ethanol by spin-coating at 3000 rpm for 40 s to remove the unbound MeO-2PACz molecules. Furthermore, the NiO_x layer was applied to the mixed-cation and mixed anion perovskite ($APbX_3$: mixture at the A site and mixture at the X site) for device evaluation.

For this purpose, 1.4 M perovskite solution was prepared by mixing formamidinium iodide (FAI), methylammonium bromide (MABr), PbI_2, $PbBr_2$, and CsI in DMF : DMSO (4 : 1, v/v) to form $Cs_{0.05}FA_{0.80}MA_{0.15}PbI_{2.75}Br_{0.25}$. The perovskite solution was then spin-coated at 1000 rpm for 10 s (200 rpm ramp) and 6000 rpm for 20 s (2000 rpm ramp). During this step, 200 μL of chlorobenzene was dropped as the antisolvent 3 s before the end of the second spin-coating process. The film was then annealed at 150 °C for 10 min. Then, PCBM and Ag were sequentially deposited as mentioned above to complete a device with the configuration of FTO/NiO_x/$Cs_{0.05}FA_{0.80}MA_{0.15}PbI_{2.75}Br_{0.25}$/PCBM/Ag with and without MeO-2PACz (*i.e.*, a SAM-modifier for the NiO_x layer).

3. Results and discussion

3.1 NiO_x thin-film characterization

Fig. S2a† shows that the sol–gel derived NiO_x thin film on top of the glass substrate has a partially ordered structure with small XRD peaks at 37.4°, 43.4°, and 63.0°, corresponding to the (111), (200), and (220) planes of NiO_x, respectively. The crystallite size (t) of NiO_x with a face-centered-cubic structure (Fig. 2Sb†) was determined using Scherrer's relation, $t = 0.9\lambda/(B\cos\theta)$, in which λ is the wavelength of X-rays (=0.154 nm), and B is a full width at

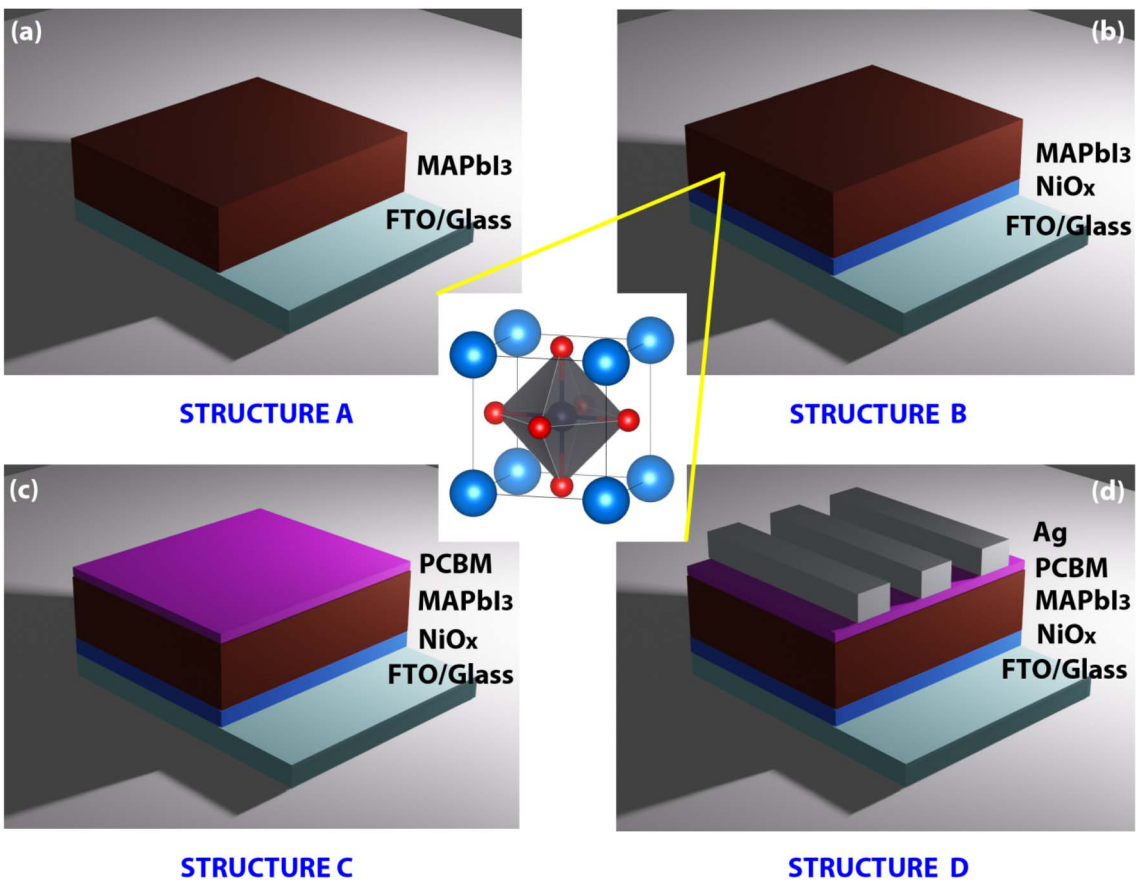

Fig. 1 Schematics of four different device structures for investigating the humid-air stress effect on the stability of perovskite solar cells: (a) structure A: FTO/$MAPbI_3$, (b) structure B: FTO/NiO_x/$MAPbI_3$, (c) structure C: FTO/NiO_x/$MAPbI_3$/PCBM and (d) structure D: FTO/NiO_x/$MAPbI_3$/PCBM/Ag. (Inset) The unit cell of $MAPbI_3$ perovskite.

half maximum (FWHM) at the diffraction angle, θ.[27] Accordingly, at the (200) crystallographic plane, the crystallite size is ~14 nm when $\lambda = 0.154$ nm, $B = 0.010647$ radian, and $\theta = 43.4°/2 = 21.7°$, respectively.

Fig. S3† shows the SEM images of (a) bare FTO and (b) the NiO_x film deposited on top of the FTO substrate, demonstrating the compact nature of a NiO_x layer with full surface coverage. Furthermore, Fig. S4† displays the AFM images of the FTO and NiO_x films, respectively. Herein, the NiO_x film exhibits a root mean square roughness of ~12.3 nm, compared to ~14.7 nm for FTO, indicating that NiO_x effectively covers the rough surface of the FTO film. Furthermore, the work function of NiO_x (acting as the HTL) was determined to be 5.21 eV (Fig. S5a†), demonstrating an appropriate energy level alignment with the surrounding layers for effective charge transport (Fig. S5b†).

3.2 Degradation analysis in humid air at room temperature

The dark storage stability was investigated for the NiO_x-based inverted $MAPbI_3$ ($MA = CH_3NH_3$) PSCs. For this purpose, all samples (unencapsulated) were stored under ambient condition at room temperature with an average relative humidity (RH) of ~60%.[40] As shown in Fig. 1, four types of device structures (a LBL approach) were employed to study the stability of each component layer under humid-air stresses.

Fig. 2 shows the stability test of four different samples under ambient conditions with RH ~ 60%. As shown in Fig. 2, up to 72 h, all samples appear similar at the initial stage. However, when the time reached 216 h, the three samples with structures A, B, and D started to fade away indicating the degradation of the perovskite layer, except the sample with structure C. For extended exposure times of up to 384 h, the samples experience significant degradation although the degree of degradation appears different. Based on these macroscopic visual images and the color change from black to yellow, we conclude decreasing sample stabilities for the structures in the order C > D > A > B.

In this stability experiment, three notable characteristics were found as follows. First, although structures A and B look

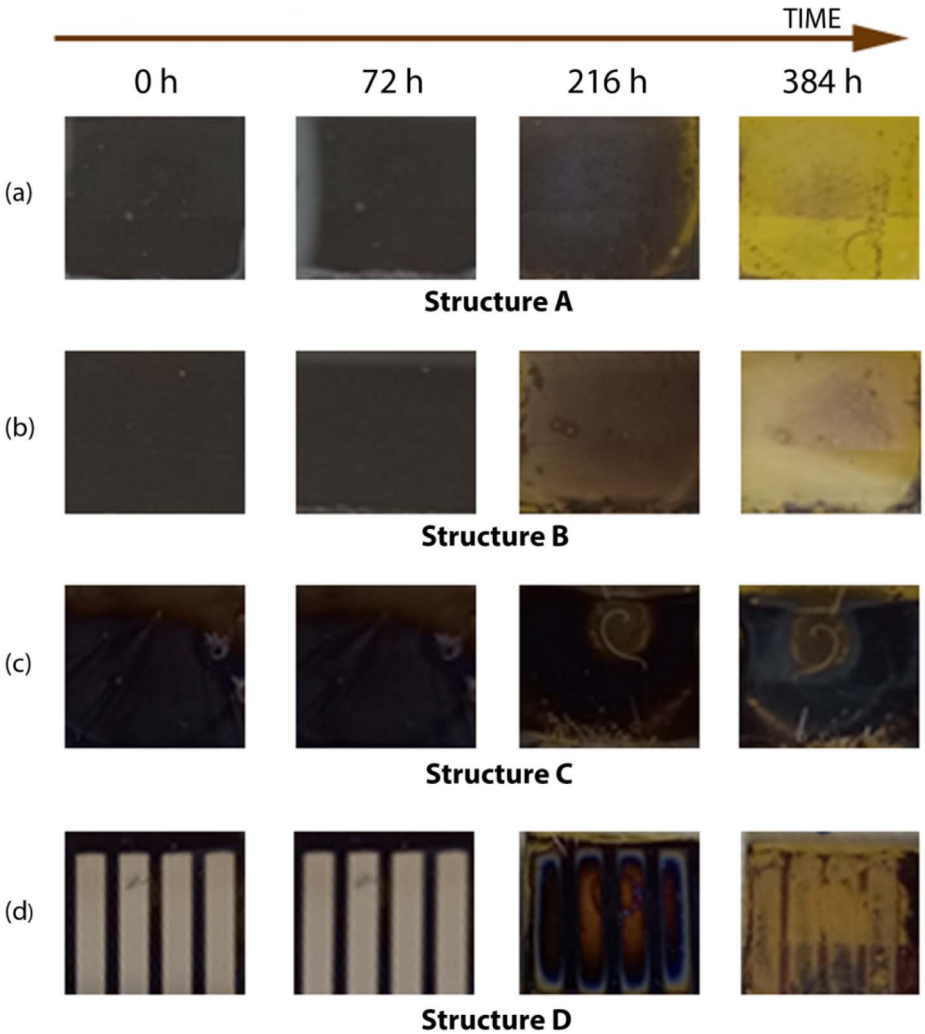

Fig. 2 Photographs showing the stability of (a) structure A: FTO/$MAPbI_3$, (b) structure B: FTO/NiO_x/$MAPbI_3$, (c) structure C: FTO/NiO_x/$MAPbI_3$/PCBM, and (d) structure D: FTO/NiO_x/$MAPbI_3$/PCBM/Ag as a function of storage time in air with a relative humidity of ~60 ± 8%. The FTO substrate size was 1.8 × 1.5 cm^2.

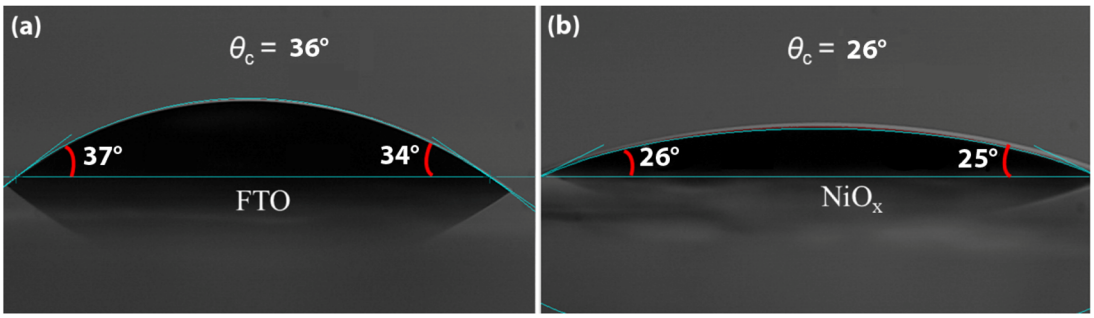

Fig. 3 Water contact angle on (a) FTO and (b) NiO_x layers, respectively.

Table 1 Water contact angle (θ_c), surface energy (γ_{sv}), and solubility parameter (δ) for the materials

	Materials for the NiO_x-based inverted perovskite solar cells				
	FTO	NiO_x	$MAPbI_3$ (ref. 27)	PCBM[42]	Ag[48]
θ_c (°)	36	26	28	75	90
γ_{sv} (mJ m^{-2})	61.5	66.4	65.5	38.2	28.3
δ ($cal^{1/2}$ $cm^{-3/2}$)	14.3	14.9	14.8	11.3	9.7
δ* ($MPa^{1/2}$)	29.3	30.5	30.3	23.2	19.9

severely degraded, structure B's black color faded away quicker than that of structure A, suggesting an influence of the underlying substrates (*i.e.* FTO and FTO/NiO_x). On measuring the water contact angle (θ_c) for these two substrates, as shown in Fig. 3, FTO showsθ_c = 36° whereas NiO_x exhibits θ_c = 26°, indicating that NiO_x is more hydrophilic than FTO. Consequently, structure B (FTO/NiO_x/$MAPbI_3$) is expected to attract more H_2O molecules from the environment with RH = 60% than structure A (FTO/$MAPbI_3$). Herein, water penetration may be considered from two directions, *i.e.*, out-of-plane (through

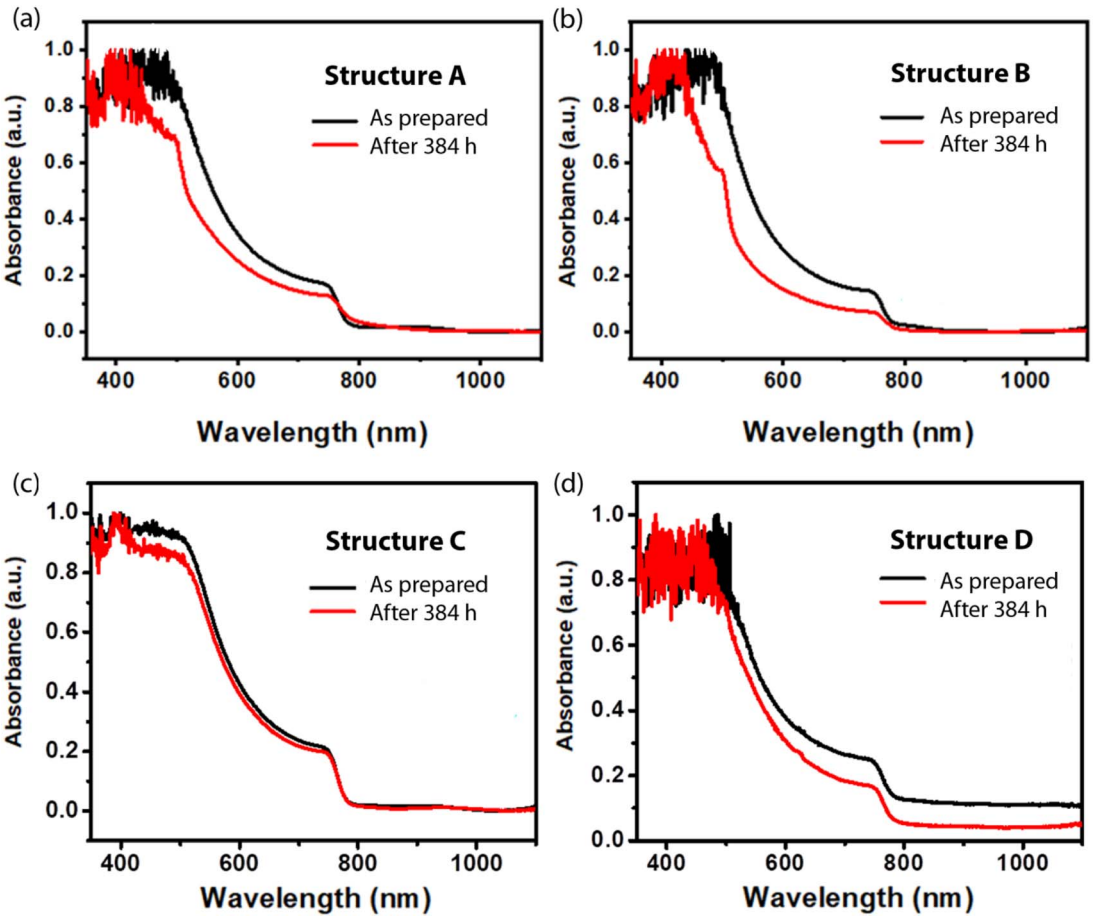

Fig. 4 UV-vis absorption of fresh samples and those after 16 days (=384 h): (a) structure A: FTO/$MAPbI_3$, (b) structure B: FTO/NiO_x/$MAPbI_3$, (c) structure C: FTO/NiO_x/$MAPbI_3$/PCBM, and (d) structure D: FTO/NiO_x/$MAPbI_3$/PCBM/Ag. The samples were exposed to oxygen and moisture with a relative humidity of ~60 ± 8%.

the perovskite surface) and in-plane (through the interface(s) between perovskite and/or underlaying layers).

Secondly, structure C (FTO/NiO_x/$MAPbI_3$/PCBM) (Fig. 2) shows superior stability amongst all samples, suggesting that PCBM serves as a passivation and protection layer in humid air, and the water penetration pathway being dominantly through the out-of-plane direction. Note that PCBM has a water contact angle $\theta_c \sim 75°$ according to the authors' previous study,[42] indicating that PCBM is less hydrophilic (low affinity for water) than FTO and NiO_x. The solid-vapor surface energy (γ_{sv}) can be calculated from Li and Neumann's relation, $\cos\theta_c = -1 + 2\sqrt{\gamma_{sv}/\gamma_{lv}}\cdot e^{-\beta(\gamma_{lv}-\gamma_{sv})^2}$, where γ_{lv} is liquid–vapor surface energy ($\gamma_{lv} = 72.75$ mJ m^{-1} for water), and β (=0.000115 m^4 mJ^{-1}) is the constant.[43,44] Then, from the relation $\delta \propto \sqrt{\gamma_{sv}}$,[42,45] we can estimate the solubility parameter of each material used for NiO_x-based inverted PSCs (see Table 1).

Third and interestingly, when the silver contacts were deposited on top of the PCBM layer, *i.e.* structure D (FTO/NiO_x/$MAPbI_3$/PCBM/Ag), the sample displayed much inferior stability to structure C (FTO/NiO_x/$MAPbI_3$/PCBM). Considering the inherent hydrophobicity of Ag with $\theta_c \sim 90°$,[46] the degradation pathway may be dominated by silver diffusion (migration), reaction with the photoactive $MAPbI_3$ layer, and leading to silver iodide formation as reported in the literature.[31,47–51] Accordingly, the silver electrode should be a critical factor affecting the instability of the NiO_x-based inverted PSCs.

Fig. 4 shows the normalized UV-vis absorption spectra for the as-prepared and 384 h-aged thin films. Here, a relative decrease in visible-light absorption is expected from the partial degradation of the photoactive $MAPbI_3$ layer with an optical bandgap of ~1.6 eV.[52,53] As expected from the stability sequence determined in Fig. 2, *i.e.* C > D > A > B, structure C displays the most stable absorption in Fig. 4c, while structure B displays the largest discrepancy between the two spectra (Fig. 4b). Notably, structure D exhibits a background shift at a wavelength ≥780 nm (non-absorption wavelength) in Fig. 4d, which is consistent with the reduced reflectivity of the metallic Ag electrodes upon their degradation.

Furthermore, the XRD patterns of the as-prepared and 384 h-aged samples were examined for characterizing their structural stability. Fig. 5 shows the peaks at (110), (112), (211), (202), (222), (312), (224) and (314) corresponding to the tetragonal phase of $MAPbI_3$.[54] For all samples aged for 348 h, the intensity of peaks was reduced, indicating the deterioration of the $MAPbI_3$ crystal. Congruently, the XRD peak at $2\theta \sim 13.0°$

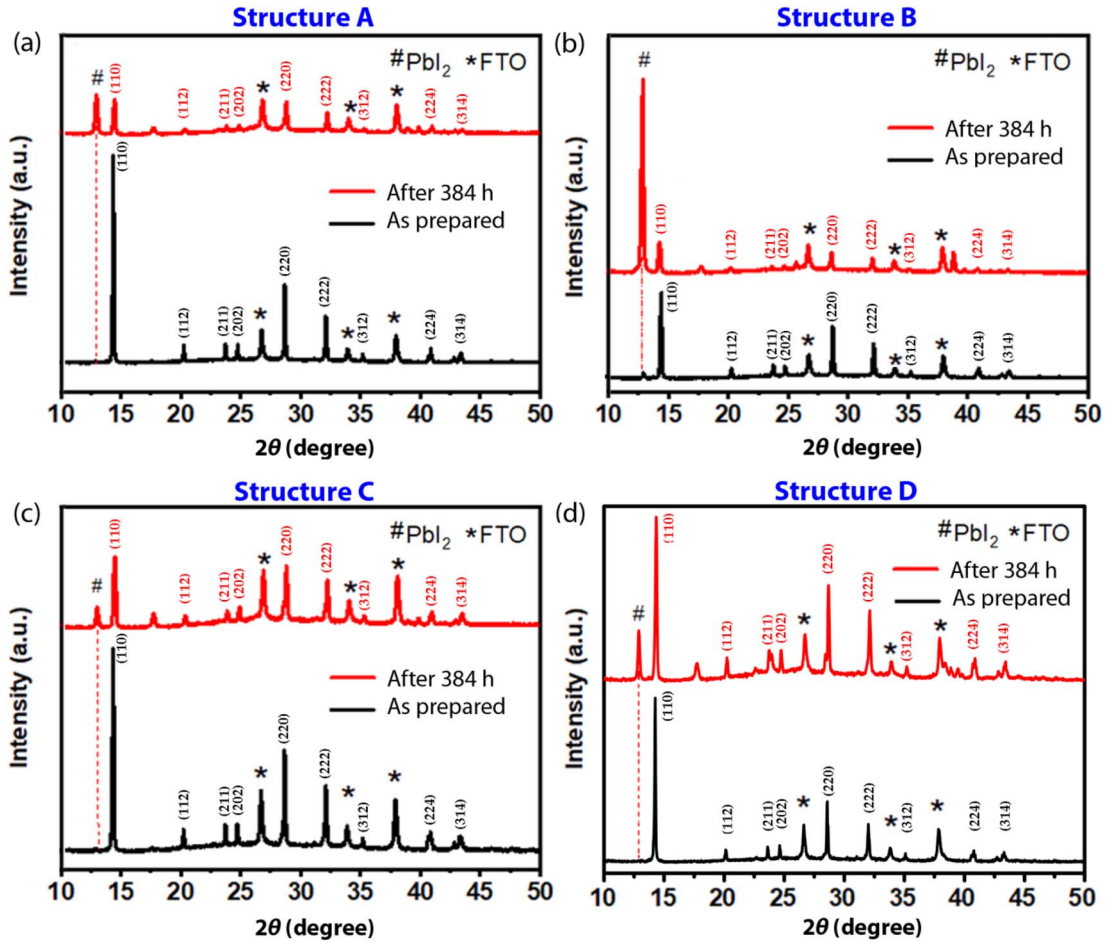

Fig. 5 XRD patterns of unencapsulated fresh samples and those after 16 days in open air (with a relative humidity of ~60 ± 8%): (a) structure A: FTO/$MAPbI_3$, (b) structure B: FTO/NiO_x/$MAPbI_3$, (c) structure C: FTO/NiO_x/$MAPbI_3$/PCBM, and (d) structure D: FTO/NiO_x/$MAPbI_3$/PCBM/Ag.

Table 2 Crystallite size of perovskite as determined from the (110) crystallographic plane in relation to various device structures and aging durations at a relative humidity of ~60 ± 8%

Device structure	Aging (h)	2θ (°)	θ (°)	β (rad)	t (nm)
A: FTO/$MAPbI_3$	0	14.4	7.2	0.00176	79.4
	384	14.5	7.3	0.00382	63.8
B: FTO/NiO_x/$MAPbI_3$	0	14.4	7.2	0.00244	57.3
	384	14.2	7.1	0.00464	52.5
C: FTO/NiO_x/$MAPbI_3$/PCBM	0	14.4	7.2	0.00215	65.0
	384	14.5	7.3	0.00424	33.0
D: FTO/NiO_x/$MAPbI_3$/PCBM/Ag	0	14.3	7.3	0.00155	90.2
	384	14.4	7.2	0.00282	45.0

developed due to the formation of a trigonal PbI_2 crystal (a decomposition product of $MAPbI_3$), displaying the (001) crystallographic plane.[55–58]

The FWHM of the (110) perovskite reflection peak was analyzed further for the as-prepared and 384 h-aged samples. Accordingly, the samples shown in Fig. 5a–d exhibited a reduction in crystallite size from (a) 79.4 nm to 63.8 nm, (b) 57.3 nm to 52.5 nm, (c) 65.0 nm to 33.0 nm, and (d) 90.2 nm to 45.0 nm, respectively (see Table 2). This result demonstrates that when the perovskite undergoes degradation, its crystallite size is diminished. In addition, the crystallite size of PbI_2 was analyzed through the (001) plane at $2\theta \sim 13°$. Table 3 shows that the samples (a), (b), (c) and (d) have a crystallite size of 33.1 nm, 34.8 nm, 34.4 nm, and 46.7 nm, respectively, with an average PbI_2 crystallite size of 37.3 ± 6.3 nm. This indicates that the $MAPbI_3$ layer underwent significant degradation *via* a reverse reaction, resulting in the formation of its crystalline precursors.

Importantly, through the ratio of the peak intensities between (001) PbI_2 and (110) $MAPbI_3$, the stability sequence of these samples could be analyzed. Accordingly, structures A, B, C, and D displayed ratios of 1.15 (=2814/2456), 6.51 (=15 608/2399), 0.28 (=754/2678), and 0.31 (=1470/4749), respectively. Hence, the structural stability sequence is 'C (0.28) > D (0.31) > A (1.15) > B (6.51)' (see Table 4) which agrees with the macroscopic assessment in Fig. 2. Here, the small ratio indicates better stability of the sample because the degradation of $MAPbI_3$ (or the formation of PbI_2) is minimized.

3.3 Device efficiency stability analysis of PSCs in humid air

We evaluated the photovoltaic performance of the sol–gel derived NiO_x HTL for inverted PSCs with the configuration of FTO/NiO_x/$MAPbI_3$/PCBM/Ag. The electrical *J–V* characteristics of the champion device are illustrated in Fig. 6a, whereas the statistical box plots of the photovoltaic parameters are summarized in Fig. S7 and Table S1 in the ESI.† A power conversion efficiency of 18.23% was achieved for the $MAPbI_3$-based solar cell.

Importantly, we assessed the performance of PSCs with the as-synthesized NiO_x as the HTL (Fig. S6†) in which perovskite was prepared *via* composition engineering. As a result, a PCE of 18.41% (based on V_{OC} ~1.1 V, J_{SC} ~21.22 mA cm^{-2} and FF ~78.50%) was achieved for the inverted PSCs with the FTO/NiO_x/$Cs_{0.05}FA_{0.80}MA_{0.15}PbI_{2.75}Br_{0.25}$/PCBM/Ag structure. Furthermore, it should be pointed out that the PSC performance can be partially enhanced by modifying NiO_x with a SAM (MeO-2PACz) treatment. For example, the power conversion efficiency was 19.56% based on V_{OC} ~1.11 V, J_{SC} ~21.99 mA cm^{-2}, and FF ~80.26%, respectively. This demonstrates that the self-assembled MeO-2PACz layer has a beneficial effect on interfacial properties in devices (Fig. S8 and Table S1†). However, the interfacial stability of SAMs in the PSC testbed needs further investigation in the future.

Then, to assess the humid-air operational stability of sol–gel derived NiO_x-based inverted PSCs, the device performance was evaluated without encapsulation at an average humidity of ~60% at room temperature. Fig. 6b displays the normalized photovoltaic performance as a function of aging time. The $MAPbI_3$-based PSCs maintained 99% of their PCE after exposure to humidity and air for the initial 4 hours. However, after exposing the device

Table 3 Crystallite size of PbI_2 at the (001) crystallographic plane as a function of the device structure in air with a relative humidity of ~60 ± 8%

Device structure	Aging (h)	2θ (°)	θ (°)	β (rad)	t (nm)
A: FTO/$MAPbI_3$	384	13.0	6.5	0.00421	33.1
B: FTO/NiO_x/$MAPbI_3$	384	12.9	6.4	0.00401	34.8
C: FTO/NiO_x/$MAPbI_3$/PCBM	384	13.0	6.5	0.00405	34.4
D: FTO/NiO_x/$MAPbI_3$/PCBM/Ag	384	12.9	6.5	0.00299	46.7

Table 4 Peak intensities and their ratio at the (001) and (110) crystallographic planes of PbI_2 and $MAPbI_3$, respectively. The samples were stored in moist air with RH ~ 60 ± 8% for 384 h

	Peak intensity (arbitrary unit)		
Device structure	(001) PbI_2	(110) $MAPbI_3$	Ratio of (001)/(110)
A: FTO/$MAPbI_3$	2814	2456	1.15
B: FTO/NiO_x/$MAPbI_3$	15 608	2399	6.51
C: FTO/NiO_x/$MAPbI_3$/PCBM	754	2678	0.28
D: FTO/NiO_x/$MAPbI_3$/PCBM/Ag	1470	4749	0.31

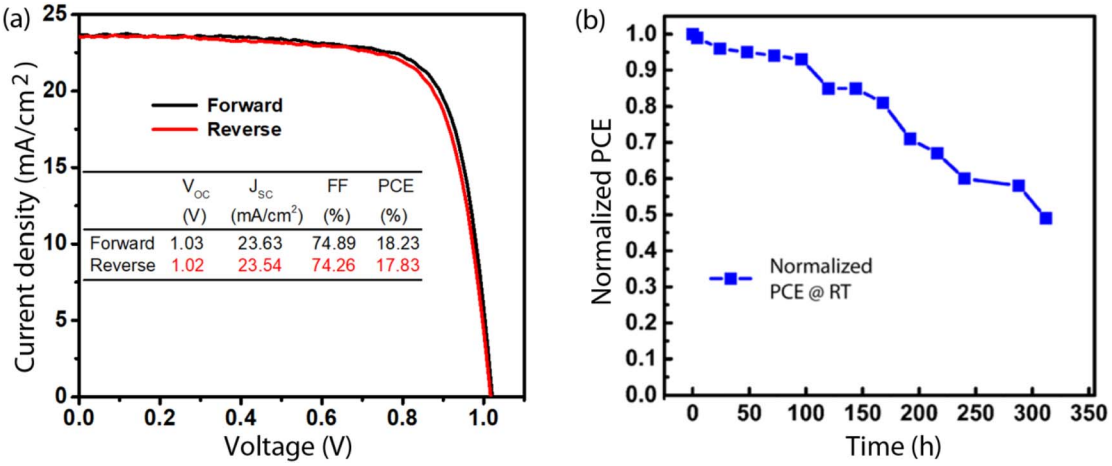

Fig. 6 Photovoltaic performance of the champion perovskite solar cells. (a) Current density *vs.* voltage (*J*–*V*) curve. (b) Efficiency evolution of the unencapsulated device (a) exposed in ambient air with a relative humidity (RH) of ~60 ± 8%.

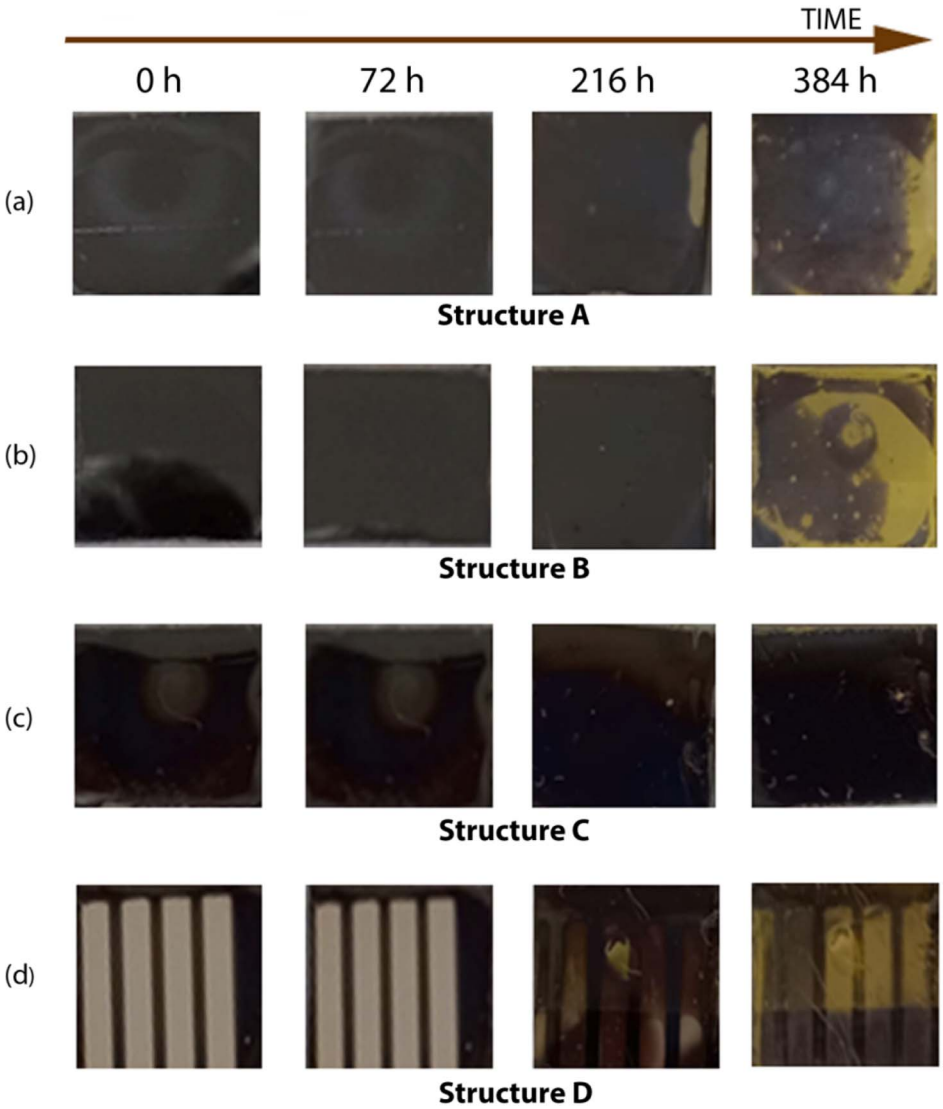

Fig. 7 Photographs of (a) structure A: FTO/$MAPbI_3$, (b) structure B: FTO/NiO_x/$MAPbI_3$, (c) structure C: FTO/NiO_x/$MAPbI_3$/PCBM, and (d) structure D: FTO/NiO_x/$MAPbI_3$/PCBM/Ag. Samples were kept unencapsulated for 16 days at 85 °C inside a nitrogen-filled glove box. The FTO substrate size is 1.8 × 1.5 cm^2.

under ambient conditions for 312 hours, the performance of PSCs showed a decline: ~49% of PCE, ~90% of J_{SC}, ~87% of V_{OC}, and ~62% of FF compared to the original values. Hence, it is noticeable that the FF decreased significantly, indicating that photo-generated charge carriers were easily recombined before being swept-out to each electrode. This should be due to the deterioration of both materials and LBL interfaces. This reveals that H_2O and O_2 molecules react mainly with $MAPbI_3$ and others 'gradually' with time based on the data trend observed in Fig. 6b. This could be further explained by the H_2O molecules wetting the $MAPbI_3$ crystals due to their hygroscopic nature[5,27] and slowly diffusing into their grains leading to the gradual decomposition of $MAPbI_3$ into its precursors, MAI and PbI_2.[59,60]

3.4 Degradation analysis under the heat stressor in a glove box

The thermal stress-induced degradation of the unencapsulated PSCs at 85 °C under dark conditions was studied in a nitrogen-filled glove box to avoid the influence of oxygen and humid air.[40] This study intended to investigate the degradation of unencapsulated devices at elevated temperatures experienced under normal operating conditions.[61] Notably, $MAPbI_3$ undergoes a phase transition from tetragonal to cubic at ~56 °C due to its polymorphism.[10,62] In general, the samples stored in a glove box at 85 °C (Fig. 7) exhibited less degradation than those samples exposed to humid air (Fig. 2). However, once again, the trend of decomposition is very similar to that of the device exposed to humidity and air as displayed in the macroscopic results (Fig. 2). Structure C (FTO/NiO_x/$MAPbI_3$/PCBM) exhibits the most robust thermal stability in this experiment. Interestingly, structure D (FTO/NiO_x/$MAPbI_3$/PCBM/Ag) in Fig. 7d shows a comparable appearance to the corresponding sample exposed to humid air in Fig. 2. Furthermore, structures A and B in Fig. 7 are more unstable than structure C,[63] indicating that PCBM serves as interfacial passivation layer for $MAPbI_3$ in the LBL structure (Fig. 1c).[64] Here, PCBM has a glass transition temperature (T_g) of ~128 °C,[42] showing that under the 85 °C condition, PCBM is in its glassy state. It should be remarked that the initial perovskite layer may have some defects (*e.g.*, grain boundaries in polycrystals)[27] due to the kinetics-driven morphology. When these defects were passivated to some extent by PCBM, the stability of $MAPbI_3$ could be enhanced toward the heat stressor. Hence, structure C is more thermally stable than structures A and B (Fig. 7). However, in the case of structure D (FTO/NiO_x/$MAPbI_3$/PCBM/Ag) as shown in Fig. 7, the silver electrode's color faded away at both 216 h and 384 h, demonstrating the detrimental effect of the heat stressor on the

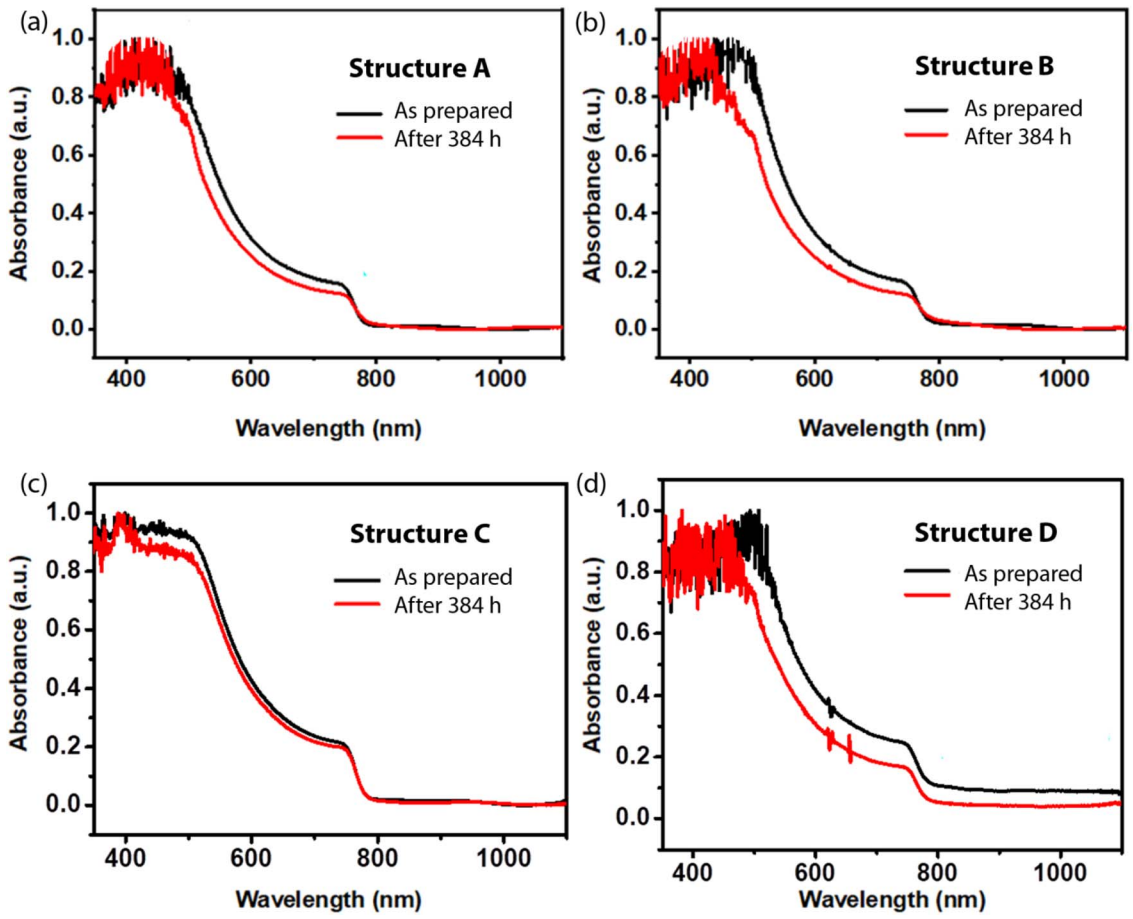

Fig. 8 UV-vis absorption spectra of (a) structure A: FTO/$MAPbI_3$, (b) structure B: FTO/NiO_x/$MAPbI_3$, (c) structure C: FTO/NiO_x/$MAPbI_3$/PCBM, and (d) structure D: FTO/NiO_x/$MAPbI_3$/PCBM/Ag. Samples were kept unencapsulated for 12 days at 85 °C in a N_2-filled glove box.

silver electrode. Moreover, silver may undergo diffusion/migration into the underlying layers at 85 °C like under exposure to humid air under ambient conditions (see Fig. 2). Li *et al.*[65] also reported that annealing a perovskite device (FTO/NiO/$MAPbI_3$/PCBM/Ag) at 85 °C causes ionic species (*e.g.*, I^-, I_2^-, and CN^-) to accumulate at the PCBM/Ag interface *via* a free volume in PCBM. Furthermore, silver can react with halide perovskite to form AgI, accelerating the perovskite degradation and resulting in device failure. At this moment, it should be remarked that the ion migration[65] in PSCs is caused to reach equilibrium between electrical and concentration gradient whether under dark or light irradiation. This phenomenon is called 'Donnan equilibrium'.[66]

Similar to Fig. 4, UV-vis absorption spectroscopy was again employed to investigate the degradation behavior of perovskite samples with thermal stress at ~85 °C in a glove box. However, it is notable that the samples were shortly exposed to ambient air conditions during this optical measurement. As displayed in Fig. 8, the trend of data is very similar to that in humid air (Fig. 4). However, the absorbance shift after 384 h aging in Fig. 8 looks relatively small compared to that in Fig. 4, indicating that the humid-air stressor is more harmful to $MAPbI_3$-based devices than the thermal stressor in this study. Furthermore, structure C (FTO/NiO_x/$MAPbI_3$/PCBM) in Fig. 8c shows a minute difference between the two absorption spectra, demonstrating the positive effect of PCBM as an interfacial passivator under thermal stress.

Fig. 9 depicts the XRD patterns for the four samples with the thermal stressor at 85 °C. First, we estimated the crystallite size at the (110) plane of $MAPbI_3$ under both the initial and 384 h-aging conditions. Accordingly, structures A, B, C, and D exhibited a reduction in crystallite size from 39.8 nm to 33.4 nm, 75.5 nm to 42.1 nm, 47.2 nm to 30.1 nm, and 79.4 nm to 34.3 nm, respectively (see Table 5). This unanimous reduction trend indicates that the $MAPbI_3$ perovskite underwent similar degradation due to the thermal stressor (here, it should be noted that all the samples were shortly exposed to air during the XRD analysis). Secondly, the formation of PbI_2 crystals was observed at $2\theta \sim 13°$, *i.e.*, the (001) plane of PbI_2, with crystallite sizes of A: 39.2 nm, B: 40.8 nm, C: 47.4 nm, and D: 34.9 nm, for the four structures, respectively, and an average crystallite size of 40.6 ± 5.2 nm (see Table 6). Additionally, from the XRD peak intensity ratio between (001) PbI_2 and (110) $MAPbI_3$ for the 384 h-aged sample, the stability sequence of each structure was estimated. As shown in Table 7, the ratio is 1.00 ≈ 2396/2402 (structure A), 1.65 ≈ 5192/3153 (structure B), 0.04 ≈ 199/4981

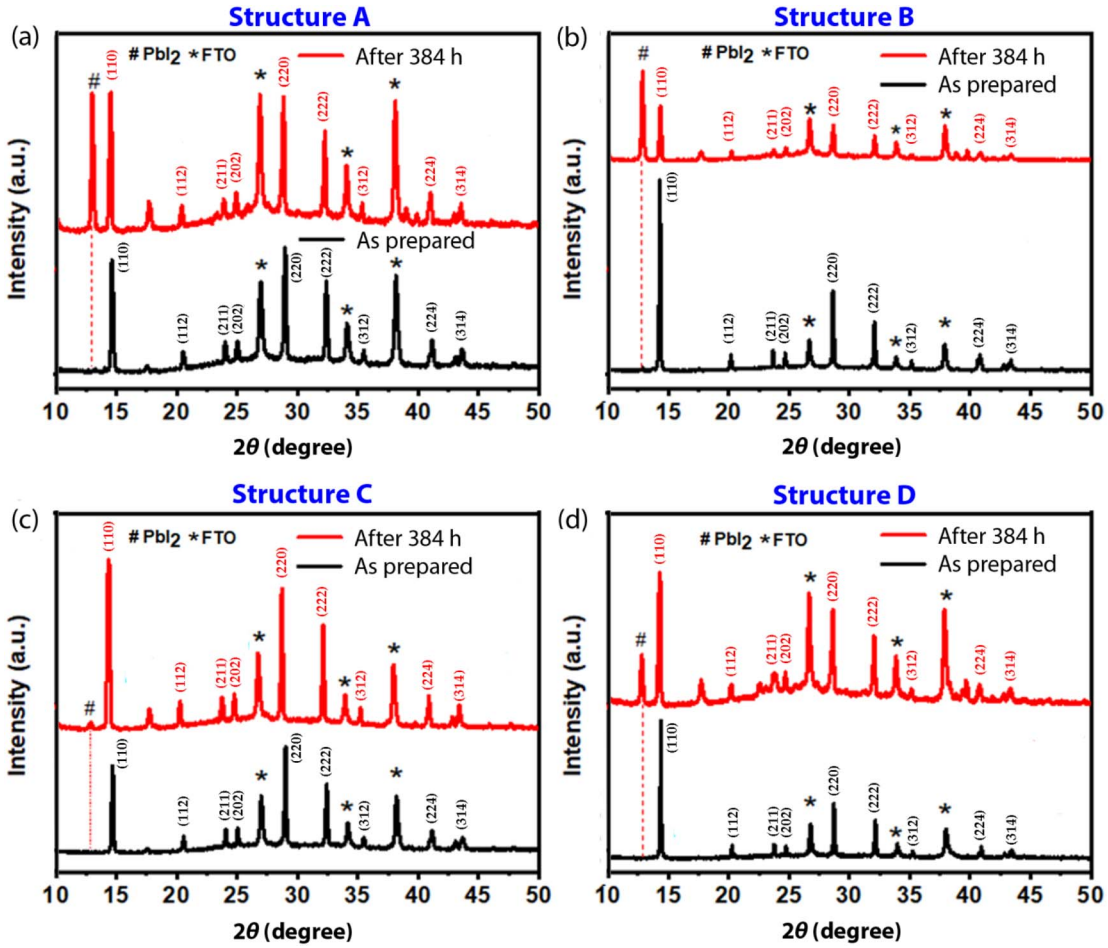

Fig. 9 XRD patterns of (a) structure A: FTO/$MAPbI_3$, (b) structure B: FTO/NiO_x/$MAPbI_3$, (c) structure C: FTO/NiO_x/$MAPbI_3$/PCBM, and (d) structure D: FTO/NiO_x/$MAPbI_3$/PCBM/Ag. The samples were kept unencapsulated for 12 days at 85 °C in a glove box.

Table 5 Crystallite size of perovskite at the (110) crystallographic plane as a function of the device structure under nitrogen-filled glove box conditions at 85 °C. XRD measurements were conducted in ambient air

Device structure	Aging (h)	2θ (°)	θ (°)	β (rad)	t (nm)
A: FTO/$MAPbI_3$	0	14.6	7.3	0.00351	39.8
	384	14.5	7.3	0.00419	33.4
B: FTO/NiO_x/$MAPbI_3$	0	14.3	7.2	0.00185	75.5
	384	14.3	7.2	0.00332	42.1
C: FTO/NiO_x/$MAPbI_3$/PCBM	0	14.7	7.4	0.00269	47.2
	384	14.3	7.2	0.00464	30.1
D: FTO/NiO_x/$MAPbI_3$/PCBM/Ag	0	14.4	7.2	0.00176	79.4
	384	14.3	7.2	0.00407	34.3

(structure C), and 0.37 ≈ 1066/2864 (structure D), respectively. Hence, the observed thermal stability sequence is 'structures C > D > A > B', which agrees with the results extracted from the humidity and air exposure.

Finally, the chemical pathways originating from thermal decomposition might be as follows:

$$MAPbI_3\ (s) \rightarrow HI\ (g) + CH_3NH_2\ (g) + PbI_2\ (s) \quad (1)$$

$$MAPbI_3\ (s) \rightarrow CH_3I\ (g) + NH_3\ (g) + PbI_2\ (s) \quad (2)$$

where eqn (1) is the kinetically favored process occurring at relatively low temperatures (76–144 °C). On the other hand, eqn (2) can be only detected at higher temperatures because of the large activation energy.[67] Hence, eqn (1) may be favored in the present work because of the relatively low-temperature condition, ~85 °C.

3.5 Photovoltaic performance stability analysis under the heat stressor in a glove box

To evaluate the thermal stability of the inverted PSCs, performance of a device fabricated under similar conditions as mentioned above was monitored within a N_2-filled glovebox at 85 °C, without encapsulation. Fig. 10a shows the *J–V* curve for the fresh device (*i.e.*, before experiencing thermal stress), whereas Fig. 10b displays the photovoltaic performance as a function of aging time at 85 °C. Notably, the normalized efficiency dramatically deteriorates within the initial four hours from 1 to 0.82 (*i.e.*, 18% loss of PCE), which is in contrast to its behavior under a humid air stressor (*e.g.*, 1% loss of PCE within 4 h). This indicates that the device was partially damaged (perhaps, *via* perovskite phase transition, atom diffusion, ion migration, defect formation, and/or decomposition) under a heat energy of ~30.85 meV ($=k_BT = 8.617 \times 10^{-5}$ eV $K^{-1} \times 358$ K, where $k_B$is the Boltzmann constant) within four hours. Then, the normalized efficiency appeared stable up to 120 h (25% loss), after which the performance rapidly declined again up to 192 h (54% loss), with a reduced slope further up to 312 h (61% loss). This significant loss is mainly due to a substantial drop in J_{SC} (only 42% remains compared to its initial value). The substantial reduction in J_{SC} should be ascribed to the diminished light harvesting of the active layer undergoing thermal degradation. The second rapid degradation after 120 h may be correlated with the Ag diffusion as proved in Fig. 7, leading to rapid performance loss of the device.

The thermal instability can be generally analyzed in terms of the perovskite materials, functional layers, interfaces, ion migration, and electrodes.[68] Here, in addition to the thermal instability of $MAPbI_3$ itself, the heat-induced silver diffusion does dramatically affect this degradation phenomenon as well. Furthermore, the photogenerated iodine (I_2) could play another role in accelerating this degradation of PSCs according to literature reports.[58,69] Besides, the volatility of organic MA^+ ions at elevated temperatures can cause irreversible structural changes in the perovskite structure under this thermal stress condition.[70] According to Ahn and Choi,[70] the $MAPbI_3$ thin films degrade at 85 °C within 24 h even under inert conditions. This indicates that heat alone can trigger the degradation of $MAPbI_3$ perovskites.

Table 6 Crystallite size of PbI_2 at the (001) crystallographic plane as a function of the device structure under nitrogen-filled glove box conditions at 85 °C. XRD measurements were conducted in ambient air

Device structure	Aging (h)	2θ (°)	θ (°)	β (rad)	t (nm)
A: FTO/$MAPbI_3$	384	13.0	6.5	0.00365	39.2
B: FTO/NiO_x/$MAPbI_3$	384	12.9	6.4	0.00342	40.8
C: FTO/NiO_x/$MAPbI_3$/PCBM	384	12.8	6.4	0.00513	47.4
D: FTO/NiO_x/$MAPbI_3$/PCBM/Ag	384	12.8	6.4	0.00400	34.9

Table 7 Peak intensities and their ratio at the (001) and (110) crystallographic planes of PbI_2 and $MAPbI_3$, respectively. The samples were stored in a glove box at 85 °C for 384 h

	Peak intensity (arbitrary unit)		
Device structure	(001) PbI_2	(110) $MAPbI_3$	Ratio of (001)/(110)
A: FTO/$MAPbI_3$	2396	2402	1.00
B: FTO/NiO_x/$MAPbI_3$	5192	3153	1.65
C: FTO/NiO_x/$MAPbI_3$/PCBM	199	4981	0.04
D: FTO/NiO_x/$MAPbI_3$/PCBM/Ag	1066	2864	0.37

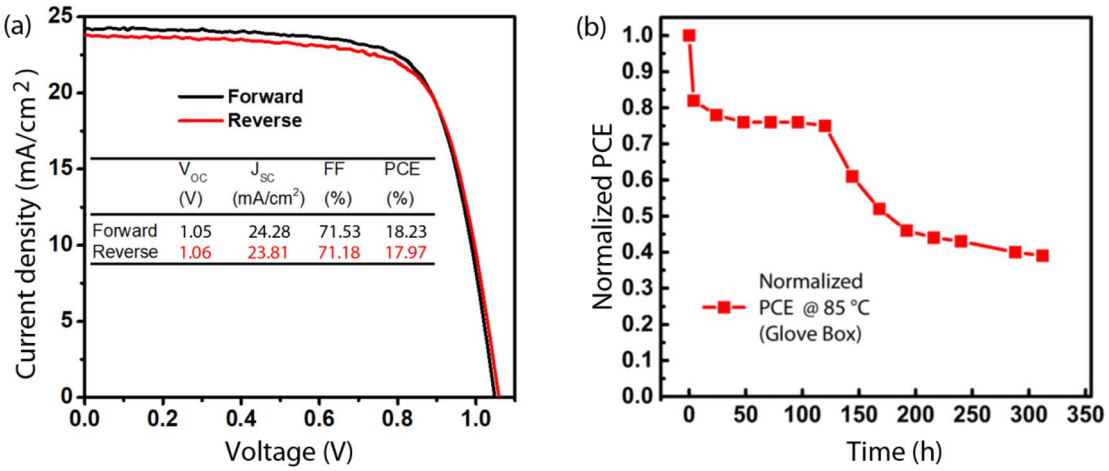

Fig. 10 Photovoltaic performance of perovskite solar cells. (a) Current density *vs.* voltage (*J*–*V*) curve of a fresh device. (b) Normalized power conversion efficiency *vs.* aging time. Here, the unencapsulated devices were exposed to 85 °C in a N_2-filled glove box.

4. Conclusions

In this study, the interfacial instability and degradation mechanism in the sol–gel-derived NiO_x-based inverted $MAPbI_3$ solar cells were elucidated. For this purpose, four different device configurations, namely (A) FTO/$MAPbI_3$, (B) FTO/NiO_x/$MAPbI_3$, (C) FTO/NiO_x/$MAPbI_3$/PCBM, and (D) FTO/NiO_x/$MAPbI_3$/PCBM/Ag were fabricated. Based on both the macroscopic and microscopic observation, the stability sequence was determined as follows, structures C > D > A > B under two external stressors (*i.e.* humid air and heat energy). Structure D was found to be inferior to structure C because of silver diffusion into the perovskite layer. Furthermore, structure B appeared slightly less stable than structure A. This may be attributed to the hydrophilicity of NiO_x, which is higher than that of FTO (the water contact angle, 25.6° *vs.* 35.8°). Importantly, the two employed external stressors affect the stability of PSCs with different kinetics. The 'humid air' affects the device stability almost linearly, whereas the 'heat energy' influences performance drastically and in a step-wise fashion. After 4 h under thermal stress, the sample shows rapid degradation to below 80% of the initial performance (likely due to perovskite phase transition), which further deteriorates after 120 h (likely due to Ag diffusion). Importantly, we demonstrated that the PCBM layer acts as an interfacial passivator for enhancing the stability of perovskite under external stressors. However, the silver diffusion into $MAPbI_3$ *via* PCBM was observed, causing perovskite degradation. Hence, the interface engineering at perovskite/PCBM/Ag layers should be imperative to enhance the lifetime of inverted PSCs with potential commercial viability. In addition, it should be also valuable to study ion migration behavior in PSCs *via* sub-nanoscale free volumes and defects (ion channels), providing a fundamental insight into device stability.

Data availability

The authors confirm that the data supporting the findings of this study are available within the ESI.†

Conflicts of interest

The authors declare no competing financial interest.

Acknowledgements

The financial support from the Jimma Institute of Technology and Mekelle University in Ethiopia is appreciated by A. T. G. A. R. U. acknowledges funding through the UBC Okanagan Principal's Research Chair program.

References

1 F. Sadegh, S. Akin, M. Moghadam, R. Keshavarzi, V. Mirkhani, M. A. Ruiz-Preciado, E. Akman, H. Zhang, M. Amini, S. Tangestaninejad, I. Mohammadpoor-Baltork, M. Graetzel, A. Hagfeldt and W. Tress, *Adv. Funct. Mater.*, 2021, **31**, 2102237, DOI: **10.1002/adfm.202102237**.
2 C. He and X. Liu, *Light Sci. Appl.*, 2023, **12**, 15, DOI: **10.1038/s41377-022-01010-4**.
3 X. Li, S. Aftab, S. Hussain, F. Kabir, A. M. A. Henaish, A. G. Al-Sehemi, M. R. Pallavolu and G. Koyyada, *J. Mater. Chem. A*, 2024, **12**, 4421–4440, DOI: **10.1039/D3TA06953B**.
4 D. A. Idosa, M. Abebe, D. Mani, J. K. Paduvilan, L. Thottathi, A. Thankappan, S. Thomas and J. Y. Kim, *Nanoscale Adv.*, 2024, **6**, 4137–4148, DOI: **10.1039/D4NA00423J**.
5 J. Y. Kim, Y. Yoo, J. Kim, W. Cho, S. Lee, Y.-E. Sung and S. Bae, *ACS Appl. Opt. Mater.*, 2024, **2**, 108–117, DOI: **10.1021/acsaom.3c00364**.
6 G. Welyab, M. Abebe, D. Mani, A. Thankappan, S. Thomas, F. G. Aga and J. Y. Kim, *Micromachines*, 2023, **14**, 1332, DOI: **10.3390/mi14071332**.
7 W. Zhang, X. Guo, Z. Cui, H. Yuan, Y. Li, W. Li, X. Li and J. Fang, *Adv. Mater.*, 2024, **36**, 2311025, DOI: **10.1002/adma.202311025**.
8 Y. Zheng, Y. Li, R. Zhuang, X. Wu, C. Tian, A. Sun, C. Chen, Y. Guo, Y. Hua, K. Meng, K. Wu and C. C. Chen, *Energy Environ. Sci.*, 2024, **17**, 1153–1162, DOI: **10.1039/d3ee03435f**.

9 J. Park, J. Kim, H. S. Yun, M. J. Paik, E. Noh, H. J. Mun, M. G. Kim, T. J. Shin and S. Il Seok, *Nature*, 2023, **616**, 724–730, DOI: 10.1038/s41586-023-05825-y.

10 H. Chen, C. Liu, J. Xu, A. Maxwell, W. Zhou, Y. Yang, Q. Zhou, A. S. R. Bati, H. Wan, Z. Wang, L. Zeng, J. Wang, P. Serles, Y. Liu, S. Teale, Y. Liu, M. I. Saidaminov, M. Li, N. Rolston, S. Hoogland, T. Filleter, M. G. Kanatzidis, B. Chen, Z. Ning and E. H. Sargent, *Science*, 2024, **384**, 189–193, DOI: 10.1126/science.adm9474.

11 E. J. Juarez-Perez, L. K. Ono, M. Maeda, Y. Jiang, Z. Hawash and Y. Qi, *J. Mater. Chem. A*, 2018, **6**, 9604–9612, DOI: 10.1039/c8ta03501f.

12 A. R. Uhl, in *Counter Electrodes for Dye-Sensitized and Perovskite Solar Cells*, ed. S. Yun and A. Hagfeldt, Wiley-VCH Verlag GmbH & Co. KGaA, Weinheim, Germany, 2018, ch. 17, pp. 421–456, DOI: 10.1002/9783527813636.ch17.

13 B. P. Kore, M. Jamshidi and J. M. Gardner, *Adv. Mater.*, 2024, **5**, 2200–2217, DOI: 10.1039/d3ma00828b.

14 N. Ahn and M. Choi, *Adv. Sci.*, 2024, **11**, 2306110, DOI: 10.1002/advs.202306110.

15 M. Casareto and N. Rolston, *Commun. Mater.*, 2024, **5**, 74, DOI: 10.1038/s43246-024-00515-2.

16 X. Lin, D. Cui, X. Luo, C. Zhang, Q. Han, Y. Wang and L. Han, *Energy Environ. Sci.*, 2020, **13**, 3823–3847, DOI: 10.1039/d0ee02017f.

17 A. Liu, X. Li, W. Zhang, H. Yang, X. Guo, C. Lu, H. Yuan, W. Ou-Yang and J. Fang, *Adv. Funct. Mater.*, 2024, **34**, 2307310, DOI: 10.1002/adfm.202307310.

18 F. Ma, Y. Zhao, J. Li, X. Zhang, H. Gu and J. You, *J. Energy Chem.*, 2021, **52**, 393–411, DOI: 10.1016/j.jechem.2020.04.027.

19 B. Li and W. Zhang, *Commun. Mater.*, 2022, **3**, 65, DOI: 10.1038/s43246-022-00291-x.

20 M. Degani, Q. An, M. Albaladejo-Siguan, Y. J. Hofstetter, C. Cho, F. Paulus, G. Grancini and Y. Vaynzof, *Sci. Adv.*, 2021, **7**, eabj7930, DOI: 10.1126/sciadv.abj7930.

21 R. Azmi, D. S. Utomo, B. Vishal, S. Zhumagali, P. Dally, A. M. Risqi, A. Prasetio, E. Ugur, F. Cao, I. F. Imran, A. A. Said, A. R. Pininti, A. S. Subbiah, E. Aydin, C. Xiao, S. Il Seok and S. De Wolf, *Nature*, 2024, **628**, 93–98, DOI: 10.1038/s41586-024-07189-3.

22 S. Zhang, F. Ye, X. Wang, R. Chen, H. Zhang, L. Zhan, X. Jiang, Y. Li, X. Ji, S. Liu, M. Yu, F. Yu, Y. Zhang, R. Wu, Z. Liu, Z. Ning, D. Neher, L. Han, Y. Lin, H. Tian, W. Chen, M. Stolterfoht, L. Zhang, W.-H. Zhu and Y. Wu, *Science*, 2023, **380**, 404–409, DOI: 10.1126/science.adg3755.

23 Z. Li, X. Sun, X. Zheng, B. Li, D. Gao, S. Zhang, X. Wu, S. Li, J. Gong, J. M. Luther, A. Li and Z. Zhu, *Science*, 2023, **382**, 284–289, DOI: 10.1126/science.ade9637.

24 A. T. Gidey, D.-W. Kuo, A. D. Fenta, C.-T. Chen and C.-T. Chen, *ACS Appl. Energy Mater.*, 2021, **4**, 6486–6499, DOI: 10.1021/acsaem.1c00496.

25 H. Zhang, S. Zhang, X. Ji, J. He, H. Guo, S. Wang, W. Wu, W. H. Zhu and Y. Wu, *Angew. Chem., Int. Ed.*, 2024, **63**, e202401260, DOI: 10.1002/anie.202401260.

26 M. Dussouillez, S. J. Moon, M. Mensi, C. M. Wolff, Y. Liu, J. H. Yum, B. A. Kamino, A. Walter, F. Sahli, L. Lauber, G. Christmann, K. Sivula, Q. Jeangros, C. Ballif, S. Nicolay and A. Paracchino, *ACS Appl. Mater. Interfaces*, 2023, **15**, 27941–27951, DOI: 10.1021/acsami.3c02709.

27 A. T. Gidey, E. Assayehegn and J. Y. Kim, *ACS Appl. Energy Mater.*, 2021, **4**, 6923–6932, DOI: 10.1021/acsaem.1c01020.

28 Z. Feng, M. Lee, R. Tian, R. Patterson, Y. Wang, C. Qian, K. Sun, Z. Liu, J. S. Yun, M. Xu, X. Zhang, H. Jin, M. Green, M. He, Z. Li and X. Hao, *Adv. Energy Mater.*, 2024, 2405016, DOI: 10.1002/aenm.202405016.

29 D. B. Khadka, Y. Shirai, M. Yanagida and K. Miyano, *ACS Appl. Energy Mater.*, 2021, **4**, 11121–11132, DOI: 10.1021/acsaem.1c02037.

30 X. Li, S. Fu, W. Zhang, S. Ke, W. Song and J. Fang, *Sci. Adv.*, 2020, **6**, eabd1580, DOI: 10.1126/sciadv.abd1580.

31 C. C. Boyd, R. Cheacharoen, T. Leijtens and M. D. McGehee, *Chem. Rev.*, 2019, **119**, 3418–3451, DOI: 10.1021/acs.chemrev.8b00336.

32 D. Zhang, D. Li, Y. Hu, A. Mei and H. Han, *Commun. Mater.*, 2022, **3**, 58, DOI: 10.1038/s43246-022-00281-z.

33 H. Back, G. Kim, J. Kim, J. Kong, T. K. Kim, H. Kang, H. Kim, J. Lee, S. Lee and K. Lee, *Energy Environ. Sci.*, 2016, **9**, 1258–1263, DOI: 10.1039/C6EE00612D.

34 X. Li, S. Fu, W. Zhang, S. Ke, W. Song and J. Fang, *Sci. Adv.*, 2020, **6**, eadb1580, DOI: 10.1126/sciadv.abd1580.

35 B. Li, J. Deng, K. D. G. I. Jayawardena, X. Liu, Y. Xiang, A. Ren, A. T. Oluwabi, S. Hinder, B. Putland, J. F. Watts, H. Li, S. Du, S. R. P. Silva and W. Zhang, *Small Methods*, 2024, **8**, 2300223, DOI: 10.1002/smtd.202300223.

36 M. Dussouillez, S.-J. Moon, M. Mensi, C. M. Wolff, Y. Liu, J.-H. Yum, B. A. Kamino, A. Walter, F. Sahli, L. Lauber, G. Christmann, K. Sivula, Q. Jeangros, C. Ballif, S. Nicolay and A. Paracchino, *ACS Appl. Mater. Interfaces*, 2023, **15**, 27941–27951, DOI: 10.1021/acsami.3c02709.

37 B. Li, S. Li, J. Gong, X. Wu, Z. Li, D. Gao, D. Zhao, C. Zhang, Y. Wang and Z. Zhu, *Chem*, 2024, **10**, 35–47, DOI: 10.1016/j.chempr.2023.09.002.

38 M. Alsari, A. J. Pearson, J. T-W Wang, Z. Wang, A. Montisci, N. C. Greenham, H. J. Snaith, S. Lilliu and R. H. Friend, *Sci. Rep.*, 2018, **8**, 5977, DOI: 10.1038/s41598-018-24436-6.

39 A. T. Gidey and J. Y. Kim, *J. Mater. Sci.: Mater. Electron.*, 2020, **31**, 12257–12268, DOI: 10.1007/s10854-020-03771-3.

40 X. Zhao, H. S. Kim, J. Y. Seo and N. G. Park, *ACS Appl. Mater. Interfaces*, 2017, **9**, 7148–7153, DOI: 10.1021/acsami.6b15673.

41 X. Yang, J. K. J. van Duren, M. T. Rispens, J. C. Hummelen, R. A. J. Janssen, M. A. J. Michels and J. Loos, *Adv. Mater.*, 2004, **16**, 802–806, DOI: 10.1002/adma.200306372.

42 J. Y. Kim, *Macromolecules*, 2019, **52**, 4317–4328, DOI: 10.1021/acs.macromol.9b00477.

43 D. Li and A. W. Neumann, *J. Colloid Interface Sci.*, 1990, **137**, 304–307, DOI: 10.1016/0021-9797(90)90067-X.

44 D. Li and A. W. Neumann, *J. Colloid Interface Sci.*, 1992, **148**, 190–200, DOI: 10.1016/0021-9797(92)90127-8.

45 J. Y. Kim, *J. Phys. Chem. C*, 2025, **129**, 3983–3992, DOI: 10.1021/acs.jpcc.5c00343.

46 H. Zhang, K. Li, M. Sun, F. Wang, H. Wang and A. K.-Y. Jen, *Adv. Energy Mater.*, 2021, **11**, 2102281, DOI: **10.1002/aenm.202102281**.
47 H. Bian, J. You, C. Xu, X. He, M. Wang, Y. Q. Yao, W. Zeng, P. Guo, H. Zhou, D. Lu, Z. Dai, S. Zhang and Q. Song, *J. Mater. Chem. A*, 2022, **11**, 205–212, DOI: **10.1039/d2ta06211a**.
48 H. Q. Wang, S. Wang, L. Chen, Z. Yin, S. Mei, Y. Zhong, Y. Yao, N. Li, J. Wang and W. Song, *Sol. Energy Mater. Sol. Cells*, 2021, **230**, 111278, DOI: **10.1016/j.solmat.2021.111278**.
49 J. You, L. Meng, T. Bin Song, T. F. Guo, W. H. Chang, Z. Hong, H. Chen, H. Zhou, Q. Chen, Y. Liu, N. De Marco and Y. Yang, *Nat. Nanotechnol.*, 2016, **11**, 75–81, DOI: **10.1038/nnano.2015.230**.
50 Q. Bao, X. Liu, S. Braun and M. Fahlman, *Adv. Energy Mater.*, 2014, **4**, 1301272, DOI: **10.1002/aenm.201301272**.
51 C. C. Boyd, R. Cheacharoen, K. A. Bush, R. Prasanna, T. Leijtens and M. D. McGehee, *ACS Energy Lett.*, 2018, **3**, 1772–1778, DOI: **10.1021/acsenergylett.8b00926**.
52 Z. Zhang, D. Wei, B. Xie, X. Yue, M. Li, D. Song and Y. Li, *Sol. Energy*, 2015, **122**, 97–103, DOI: **10.1016/j.solener.2015.08.028**.
53 P. Yadav, K. Pandey, P. Bhatt, D. Raval, B. Tripathi, C. P. Kanth, M. K. Pandey and M. Kumar, *Sol. Energy*, 2015, **122**, 773–782, DOI: **10.1016/j.solener.2015.09.046**.
54 X. Guo, C. McCleese, C. Kolodziej, A. C. S. Samia, Y. Zhao and C. Burda, *Dalton Trans.*, 2016, **45**, 3806–3813, DOI: **10.1039/C5DT04420K**.
55 B. Li, J. Deng, K. D. G. I. Jayawardena, X. Liu, Y. Xiang, A. Ren, A. T. Oluwabi, S. Hinder, B. Putland, J. F. Watts, H. Li, S. Du, S. Ravi, P. Silva and W. Zhang, *Small Methods*, 2024, **8**, 230223, DOI: **10.1002/smtd.202300223**.
56 S. M. Feyadh and A. H. Mohammed, *Mater. Res. Express*, 2022, **9**, 055402, DOI: **10.1088/2053-1591/ac6d4b**.
57 A. Liu, X. Li, W. Zhang, H. Yang, X. Guo, C. Lu, H. Yuan, W. Ou-Yang and J. Fang, *Adv. Funct. Mater.*, 2024, **34**, 2307310, DOI: **10.1002/adfm.202307310**.
58 J. Thiesbrummel, S. Shah, E. Gutierrez-Partida, F. Zu, F. Peña-Camargo, S. Zeiske, J. Diekmann, F. Ye, K. P. Peters, K. O. Brinkmann, P. Caprioglio, A. Dasgupta, S. Seo, F. A. Adeleye, J. Warby, Q. Jeangros, F. Lang, S. Zhang, S. Albrecht, T. Riedl, A. Armin, D. Neher, N. Koch, Y. Wu, V. M. Le Corre, H. Snaith and M. Stolterfoht, *Nat. Energy*, 2024, **9**, 664–676, DOI: **10.1038/s41560-024-01487-w**.
59 V. Nalini, G. N. Nagy, A. Rahaman, S. K. Kalpathy, T. Thomas, T. P. Sumangala and M. U. Kahaly, *Adv. Mater.*, 2024, **5**, 6426, DOI: **10.1039/d4ma00574k**.
60 B. P. Kore, M. Jamshidi and J. M. Gardner, *Adv. Mater.*, 2024, **5**, 2200–2217, DOI: **10.1039/d3ma00828b**.
61 W. C. Lin, W. C. Lo, J. X. Li, P. C. Huang and M. Y. Wang, *ACS Omega*, 2021, **6**, 34606–34614, DOI: **10.1021/acsomega.1c05002**.
62 A. Alaei, A. Circelli, Y. Yuan, Y. Ying and S. S. Lee, *Adv. Mater.*, 2021, **2**, 47, DOI: **10.1039/D0MA00643B**.
63 C. C. Boyd, R. C. Shallcross, T. Moot, R. Kerner, L. Bertoluzzi, A. Onno, S. Kavadiya, C. Chosy, E. J. Wolf, J. Werner, J. A. Raiford, C. de Paula, A. F. Palmstrom, Z. J. Yu, J. J. Berry, S. F. Bent, Z. C. Holman, J. M. Luther, E. L. Ratcliff, N. R. Armstrong and M. D. McGehee, *Joule*, 2020, **4**, 1759–1775, DOI: **10.1016/j.joule.2020.06.004**.
64 W. Shen, Y. Dong, F. Huang, Y.-B. Cheng and J. Zhong, *Mater. Rep.: Energy*, 2021, **1**, 10060, DOI: **10.1016/j.matre.2021.100060**.
65 J. Li, Q. Dong, N. Li and L. Wang, *Adv. Energy Mater.*, 2017, **7**, 1602922, DOI: **10.1002/aenm.201602922**.
66 F. G. Donnan, *Chem. Rev.*, 1924, **1**, 73–90, DOI: **10.1021/cr60001a003**.
67 S. Kundu and T. L. Kelly, *EcoMat*, 2020, **2**, e12025, DOI: **10.1002/eom2.12025**.
68 D. Zhang, D. Li, Y. Hu, A. Mei and H. Han, *Commun. Mater.*, 2022, **3**, 58, DOI: **10.1038/s43246-022-00281-z**.
69 X. Ma, R. Luo, X. Li, H. Yu, J. Huang, W. Yang, H. Shi, Y. Shen and M. Wang, *Mater. Today Phys.*, 2025, **50**, 101616.
70 N. Ahn and M. Choi, *Adv. Sci.*, 2024, **11**, 2306110, DOI: **10.1002/advs.202306110**.